LETTER

https://doi.org/10.1038/s41586-019-1031-8

Observation of unconventional chiral fermions with long Fermi arcs in CoSi

Zhicheng Rao[1,2,8], Hang Li[1,2,8], Tiantian Zhang[1,2,8], Shangjie Tian[3,8], Chenghe Li[3], Binbin Fu[1,2], Cenyao Tang[1,2], Le Wang[1,2], Zhilin Li[1,4], Wenhui Fan[1,2], Jiajun Li[1,2], Yaobo Huang[5], Zhehong Liu[1,2], Youwen Long[1,6], Chen Fang[1,6,7], Hongming Weng[1,2,6,7], Youguo Shi[1,6], Hechang Lei[3]*, Yujie Sun[1,6,7]*, Tian Qian[1,6,7]* & Hong Ding[1,6,7]

Chirality—the geometric property of objects that do not coincide with their mirror image—is found in nature, for example, in molecules, crystals, galaxies and life forms. In quantum field theory, the chirality of a massless particle is defined by whether the directions of its spin and motion are parallel or antiparallel. Although massless chiral fermions—Weyl fermions—were predicted 90 years ago, their existence as fundamental particles has not been experimentally confirmed. However, their analogues have been observed as quasiparticles in condensed matter systems. In addition to Weyl fermions[1–4], theorists have proposed a number of unconventional (that is, beyond the standard model) chiral fermions in condensed matter systems[5–8], but direct experimental evidence of their existence is still lacking. Here, by using angle-resolved photoemission spectroscopy, we reveal two types of unconventional chiral fermion—spin-1 and charge-2 fermions—at the band-crossing points near the Fermi level in CoSi. The projections of these chiral fermions on the (001) surface are connected by giant Fermi arcs traversing the entire surface Brillouin zone. These chiral fermions are enforced at the centre or corner of the bulk Brillouin zone by the crystal symmetries, making CoSi a system with only one pair of chiral nodes with large separation in momentum space and extremely long surface Fermi arcs, in sharp contrast to Weyl semimetals, which have multiple pairs of Weyl nodes with small separation. Our results confirm the existence of unconventional chiral fermions and provide a platform for exploring the physical properties associated with chiral fermions.

In high-energy physics, the standard model predicts three types of fermionic particle in the Universe —Dirac, Weyl and Majorana fermions—on the basis of the Poincaré group. Condensed matter systems can realize a variety of fermionic quasiparticles at topological nodes (that is, robust band-crossing points protected from being gapped by nontrivial band topology[1–16]), which may or may not have analogues in high-energy physics. Chiral fermions in condensed matter systems exist at nodes that carry a non-zero Chern number, which dictates that the surface states have a helicoid band structure surrounding the surface projections of the nodes. The equal-energy contours of such helicoid surface states are topologically robust Fermi arcs connecting the surface projections of nodes with opposite Chern numbers.

So far, angle-resolved photoemission spectroscopy (ARPES) experiments have verified three types of fermion at the topological nodes: twofold-degenerate Weyl nodes[17–20], fourfold-degenerate Dirac nodes[21] and threefold-degenerate nodes[22,23]. The Chern number is zero for Dirac nodes and undefined for threefold-degenerate nodes. Only the Weyl nodes carry non-zero Chern number, $C = \pm 1$. The non-zero Chern number causes the Weyl fermion excitations at the nodes to have chirality and necessitates the presence of exotic helicoid surface states with Fermi arcs as their equal-energy contours.

Topological nodes can be classified as either accidental or essential. The three types of experimentally identified node are all accidental because they require band inversion, and they are stabilized by certain symmorphic crystal symmetries or nontrivial topology. By contrast, band theory has shown several types of essential node with multiple band crossings that do not require band inversion. These are enforced at high-symmetry momenta in the Brillouin zone (BZ) by specific crystal symmetries, at which the number of degenerate bands corresponds to the dimension of irreducible representations of the little group (a set of symmetry operators that leave the k point invariant).

Theorists have proposed exotic chiral fermions at essential nodes with non-zero Chern numbers, such as spin-1 nodes with threefold degeneracy[5,6], charge-2 Dirac nodes and spin-3/2 Rarita–Schwinger–Weyl nodes with fourfold degeneracy[6–8], and double-spin-1 nodes with sixfold degeneracy[5–8]. Unlike Weyl fermions, these chiral fermions have no analogues in high-energy physics and thus are unconventional (that is, beyond the standard model). Although first-principles calculations have suggested the presence of these unconventional chiral fermions in numerous materials[5–8], experimental evidence is still lacking. In this work, we experimentally verified the presence of chiral spin-1 fermions and charge-2 fermions in the transition-metal silicide CoSi by investigating the electronic band structures of both its bulk and surface states with systematic ARPES measurements.

Figure 1a illustrates the crystal structure of CoSi, in which each Co atom is bonded with six Si atoms and vice versa, forming a simple cubic structure with lattice constant $a = 4.445$ Å and space group $P2_13$ (number 198). The corresponding BZ in Fig. 1b is also simple cubic with four high-symmetry momentum points Γ, X, M and R. First-principles calculations[6] have shown that the band structure has a threefold-degenerate point at Γ and a fourfold-degenerate point at R near the Fermi level (E_F) (Fig. 1e) when spin–orbit coupling (SOC) is not considered. Similar degenerate points have also been identified in the phonon spectra[24] of CoSi. When considering SOC, the bands split owing to the absence of inversion symmetry. However, the band splitting is of the order of millielectronvolts because of the weak SOC on the Co 3d and Si 3p orbitals[8]. Thus, the SOC effects can be ignored in experimental work.

Unlike the experimentally verified threefold-degenerate nodes[22,23] and Dirac nodes[21], the nodes at Γ and R in CoSi carry non-zero Chern numbers[6,24] of ± 2, where the quasiparticle excitations are described as chiral spin-1 fermions and charge-2 fermions, respectively. According to the no-go theorem, the spin-1 and charge-2 nodes in CoSi must have opposite Chern numbers and are expected to have two surface Fermi arcs connecting their projections on certain surfaces. Considering the

[1]Beijing National Laboratory for Condensed Matter Physics and Institute of Physics, Chinese Academy of Sciences, Beijing, China. [2]University of Chinese Academy of Sciences, Beijing, China. [3]Department of Physics and Beijing Key Laboratory of Opto-electronic Functional Materials and Micro–nano Devices, Renmin University of China, Beijing, China. [4]State Key Laboratory for Artificial Microstructure and Mesoscopic Physics, Beijing Key Laboratory of Quantum Devices, Peking University, Beijing, China. [5]Shanghai Synchrotron Radiation Facility, Shanghai Institute of Applied Physics, Chinese Academy of Sciences, Shanghai, China. [6]Songshan Lake Materials Laboratory, Dongguan, China. [7]CAS Centre for Excellence in Topological Quantum Computation, University of Chinese Academy of Sciences, Beijing, China. [8]These authors contributed equally: Zhicheng Rao, Hang Li, Tiantian Zhang, Shangjie Tian. *e-mail: hlei@ruc.edu.cn; yjsun@iphy.ac.cn; tqian@iphy.ac.cn

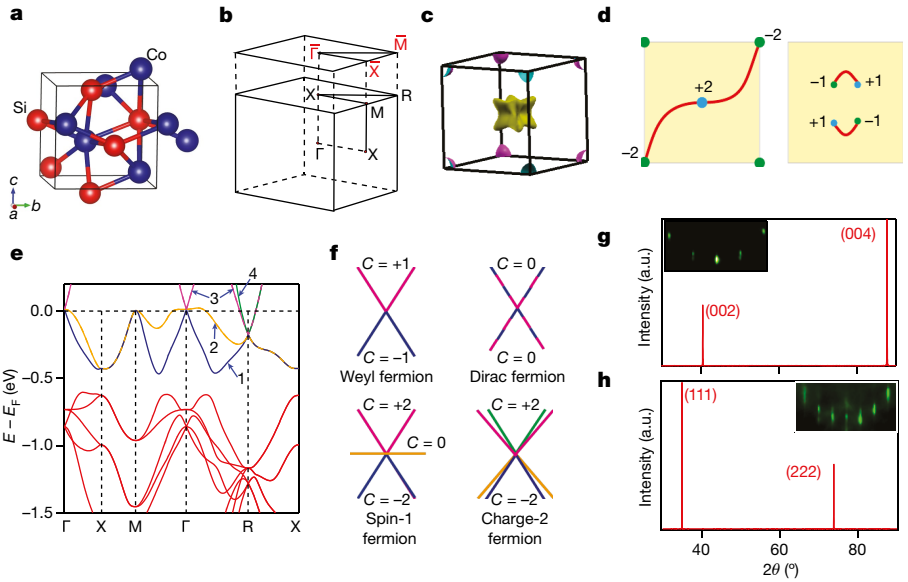

Fig. 1 | Crystal structure and calculated electronic structure of CoSi. **a**, Crystal structure of CoSi. **b**, Bulk BZ and (001) surface BZ of CoSi. The high-symmetry momentum points are indicated. **c**, Calculated FSs in the bulk BZ. **d**, Schematics of the Fermi arcs connecting the projections of two nodes with opposite chiralities for CoSi (left) and Weyl semimetals (right). **e**, Calculated bulk band structure along high-symmetry lines without SOC. **f**, Schematics of the band structures of a Weyl fermion, a Dirac fermion, a spin-1 fermion and a charge-2 fermion. **g**, X-ray diffraction pattern measured on the (001) plane of CoSi. The inset shows the RHEED pattern of CoSi after repeated sputtering and annealing. **h**, Same as **g** but measured on the (111) plane. a.u., arbitrary units.

band structure of CoSi shown in Fig. 1e, the Fermi arcs should lie in the gap between bands 2 and 3. As shown in Fig. 1c, these bands form the hole- and electron-like Fermi surfaces (FSs) that enclose the spin-1 and charge-2 nodes, respectively, leaving a large direct gap between them in regions other than the FSs. This is important for the observation of surface Fermi arcs near E_F.

As illustrated in Fig. 1d, the nodes in CoSi are projected onto the centre or corner of the (001) surface BZ. The expected Fermi arcs connecting them traverse a distance of about 1 $Å^{-1}$, which is more than ten times larger than those in the Weyl semimetals TaAs[17,18] and $MoTe_2$[19,20]. Moreover, the Weyl nodes can shift by external conditions, such as the SOC strength, lattice constants and atom positions, and even merge together, leading to annihilation of Weyl nodes. By contrast, the spin-1 and charge-2 nodes in CoSi are enforced at the high-symmetry momentum points Γ and R, and they appear more robust than the Weyl nodes, unless the related crystal symmetries are altered.

Because the Co and Si atoms are strongly bonded by multiple covalent bonds in three dimensions, it is almost unfeasible to obtain atomically flat surfaces for ARPES measurements by cleaving single crystals. We therefore tried to polish the surfaces of single crystals and then repeatedly sputtered and annealed the polished surfaces in vacuum. Eventually, we attained atomically flat (111) and (001) surfaces, as manifested by the clear reflection high-energy electron diffraction (RHEED) patterns in the insets of Fig. 1g, h.

In ARPES experiments, photoelectrons excited by soft X-rays have a much longer escape depth than those excited with vacuum ultraviolet (VUV) light. We thus can selectively probe the bulk and surface states using soft X-rays and VUV light. The ARPES data collected with soft X-rays on the (111) surface are summarized in Fig. 2. By varying the photon energy ($h\nu$; h, Planck constant; ν, frequency), we obtain the band dispersions along Γ–R, which is normal to the (111) surface, as shown in Fig. 2d. We observed two hole-like bands around Γ near E_F, which degenerate with an electron-like band at R. We further investigated the in-plane band structure on the (111) surface with $h\nu = 435$ eV, which characterizes the momentum plane containing the R and X points, as illustrated in Fig. 2a, b. We observed a circular FS patch at R (Fig. 2c), which arises from the electron-like band shown in Fig. 2e, f. This electron-like band degenerates with a relatively flat band about 0.2 eV below E_F at R. All the observations on the (111) surface are consistent with the calculated bulk band structures, except that the splitting of the electron-like band along Γ–R is not resolved.

The ARPES data collected with soft X-rays on the (001) surface are summarized in Fig. 3. We plot in Fig. 3d, e the FSs measured with $h\nu = 355$ eV and 300 eV, respectively. The experimental FS at the BZ centre in Fig. 3d is consistent with the calculated hole-like FS at Γ in Fig. 3b, whereas the FS at the BZ corner in Fig. 3e is consistent with

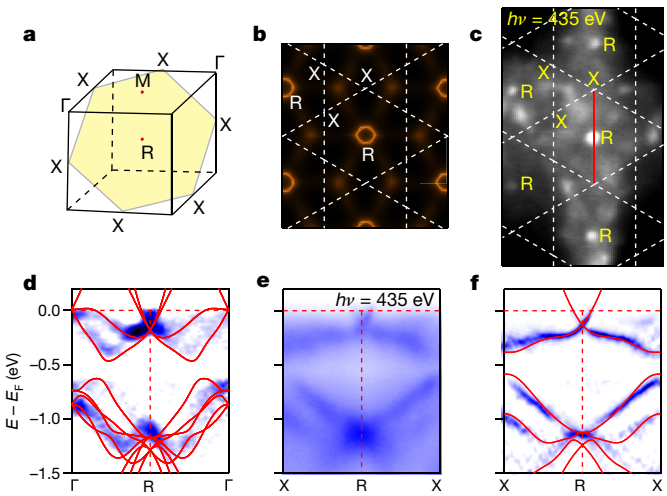

Fig. 2 | Fermi surfaces and band dispersions measured on the (111) surface. **a**, The hexagon in the three-dimensional BZ indicates the (111) plane that contains the R and X points. **b**, **c**, Calculated (**b**) and experimental (**c**) intensity plots at E_F, showing the FSs in the (111) plane indicated in **a**. Dashed lines represent the intersecting lines of the (111) plane and the bulk BZ boundary. **d**, Curvature intensity plot of the ARPES data measured with varying $h\nu$ from 325 eV to 580 eV, showing the band dispersions along R–Γ–R. The inner potential was set at 27 eV to fit the periodicity of band dispersions along R–Γ–R. **e**, **f**, Intensity (**e**) and curvature intensity (**f**) plots of the ARPES data along X–R–X. For comparison, we plot the calculated bands along R–Γ–R and X–R–X as red lines on top of the experimental data in **d** and **f**, respectively. The ARPES data in **c**, **e** and **f** were collected with $h\nu = 435$ eV.

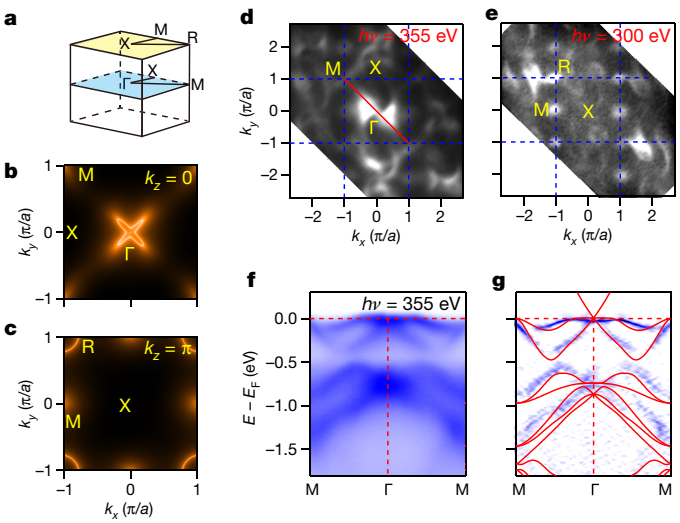

Fig. 3 | Fermi surfaces and band dispersions measured with soft X-rays on the (001) surface. a, Three-dimensional bulk BZ with the $k_z = 0$ and π planes indicated by cyan and yellow colours, respectively. **b**, **c**, Calculated bulk FSs in the $k_z = 0$ (**b**) and $k_z = π$ (**c**) planes. **d**, **e**, ARPES intensity maps at E_F, measured with $hν = 355$ eV (**d**) and 300 eV (**e**). **f**, **g**, Intensity (**f**) and curvature intensity (**g**) plots of the ARPES data along M–Γ–M collected with $hν = 355$ eV. For comparison, we plot the calculated bands along M–Γ–M as red lines on top of the experimental data in **g**.

the calculated electron-like FS at R in Fig. 3c. This indicates that the measured momenta in Fig. 3d, e correspond to the $k_z = 0$ and $k_z = π$ planes, respectively. Figure 3f, g shows the experimental band dispersions measured with $hν = 355$ eV, which are consistent with the calculated bands along Γ–M.

The excellent consistency between experiment and calculation provides solid evidence for the presence of spin-1 and charge-2 nodes in the bulk of CoSi. Because these nodes have non-zero Chern numbers, it is expected that surface Fermi arcs emanate from their projections on certain surfaces. At the (111) surface, the nodes at Γ and R are projected onto the same point at the surface BZ centre, where their Chern numbers cancel each other out. There are no topological surface states on the (111) surface. By contrast, at the (001) surface, the Γ and R points are projected onto the centre $\overline{\Gamma}$ and corner $\overline{M}$ of the surface BZ, respectively (see Fig. 1b). It is therefore expected that two Fermi arcs connect the $\overline{\Gamma}$ and $\overline{M}$ points on the (001) surface.

In Fig. 3d, e we observe some extra features in the soft-X-ray ARPES data compared with the calculated bulk FSs. These features may come from the (001) surface states. To confirm this, we carried out APRES experiments on the (001) surface using VUV light. The VUV ARPES data collected on the (001) surface are summarized in Fig. 4. The extra features at E_F are more clearly observed in the VUV ARPES data in Fig. 4a, b. Their momentum locations do not change with varying photon energy of the incident light (see left panel of Fig. 4e), proving their surface origin. The most remarkable feature in the surface states is that two Fermi arcs traverse the (001) surface BZ to connect the bulk FS pockets at $\overline{\Gamma}$ and $\overline{M}$. The two Fermi arcs are related by a π rotation about $\overline{\Gamma}$, which is constrained by time-reversal symmetry because the lattice symmetries in the bulk are broken at the (001) surface.

By analysing the surface states, we can reveal the topological nature of the bulk nodes in CoSi. As we know, the surface projection of a bulk node with a non-zero Chern number is surrounded by helicoid surface states[25]. These states have chiral band dispersions on the loop that encircles the projection of the node, and their equal-energy contours are robust Fermi arcs connecting the projections of nodes with opposite chiralities, as schematically illustrated in Fig. 4i. In Fig. 4h, we show the band dispersions of the surface states on loops 1 and 2, which encircle points $\overline{\Gamma}$ and $\overline{M}$, respectively, as indicated in Fig. 4b. On loop 2, we observe two surface bands crossing E_F with the same chirality. On loop 1, the surface bands pass through E_F six times—four times with the same chirality and two with the opposite chirality. Therefore, the net count on loop 1 is two. There should be only two surface bands with the same chirality on loop 1. Each band first goes up through E_F, then returns below E_F, and finally goes up through E_F again. We note that

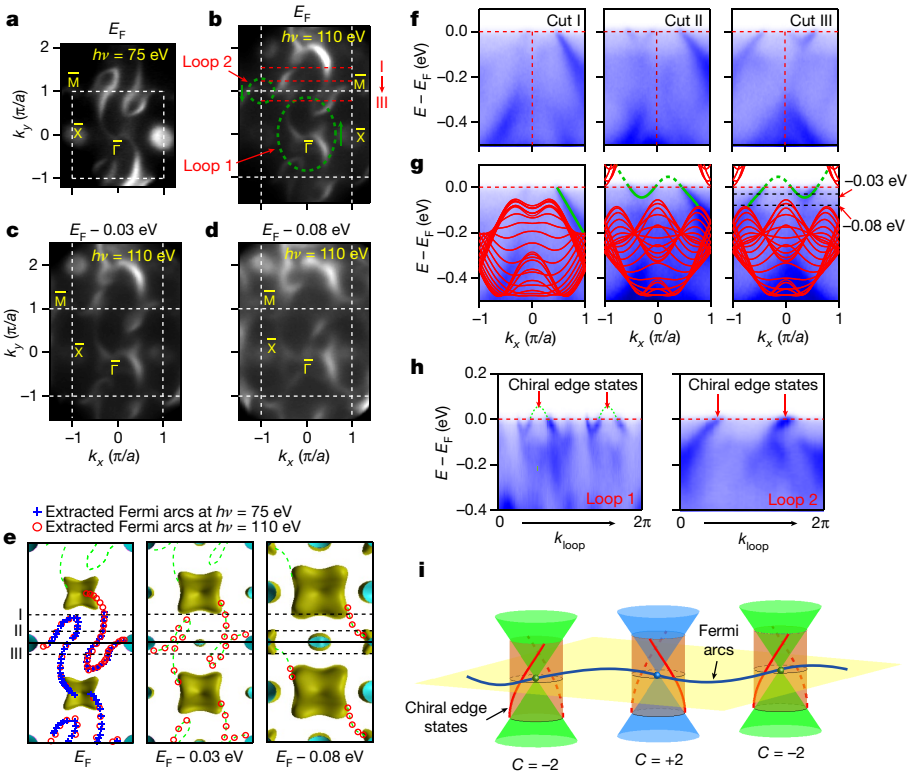

Fig. 4 | Surface Fermi arcs measured with VUV light on the (001) surface. a, ARPES intensity map at E_F, measured with $hν = 75$ eV. **b**–**d**, ARPES intensity maps at E_F (**b**), $E_F - 0.03$ eV (**c**) and $E_F - 0.08$ eV (**d**), measured with $hν = 110$ eV. The momentum locations of loops 1 and 2 and cuts I, II and III are indicated in **b**. **e**, Surface Fermi arcs extracted from the ARPES intensity maps at E_F (left), $E_F - 0.03$ eV (middle) and $E_F - 0.08$ eV (right), showing the connection between the (001) surface projections of the bulk FSs at $\overline{\Gamma}$ and $\overline{M}$. The dashed lines indicate the momentum locations of cuts I, II and III. **f**, ARPES intensity plots showing the band dispersions along cuts I, II and III. For comparison, we plot the projections of the calculated bulk bands as red lines on top of the experimental data in **g**. Solid and dashed green lines in **g** are guides for the eye for the surface state bands. **h**, ARPES intensity plots showing the band dispersions on loops 1 and 2. **i**, Schematic showing chiral edge states on the loops that encircle the surface projections of bulk nodes with non-zero Chern numbers $C = ±2$ and surface Fermi arcs connecting the surface projections of bulk nodes with opposite chiralities.

the surface bands on the two loops have opposite chiralities. These results provide sufficient evidence that the two bulk nodes at Γ and R have opposite Chern numbers, $C = \pm 2$.

To further illuminate the nontrivial topology, we show the band dispersions along three cuts—I, II and III—in Fig. 4f, g. Along cut I, one surface band passes through E_F once. Along cuts II and III, one surface band passes through E_F three times, similarly to the case of loop 1. The chirality of the surface band along cut III is opposite to that of the bands along cuts I and II, indicating that they have opposite Chern numbers, $C = \pm 1$. When sliding the horizontal cut in the vertical direction, when the cut passes through points $\overline{\Gamma}$ or $\overline{M}$ the Chern number must be changed by $+2$ or -2, which correspond to the Chern numbers of the bulk nodes.

The nontrivial surface states form topologically robust surface Fermi arcs at constant energy, which connect the surface projections of the spin-1 and charge-2 nodes. Figure 4a–e shows that although the Fermi arcs are dramatically deformed with varying the constant energy, the connection between $\overline{\Gamma}$ and $\overline{M}$ is not destroyed. This is essentially distinct from the Fermi arcs observed in Na_3Bi (ref. [26]) and WC (ref. [23]), where the Fermi arcs continuously deform into closed FSs separated from the bulk states by varying the constant energy[25,27]. The unprotected Fermi arcs indicate that the normal Dirac nodes in Na_3Bi and the threefold-degenerate nodes in WC have no chirality.

Through systematic characterization and analysis of the band structures of the bulk and surface states of CoSi, we have unambiguously proven that the nodes at Γ and R in CoSi have non-zero Chern numbers, at which fermionic excitations have chirality. This is the first direct experimental evidence of the presence of unconventional chiral fermions beyond Weyl fermions in condensed matter systems. Compared with Weyl fermions, these unconventional chiral fermions have many distinct characteristics. They usually lie at time-reversal-invariant momentum points and are unrelated by symmetry, which is conducive to the realization of three-dimensional time-reversal-invariant topological superconductivity because FSs with opposite Chern numbers must have opposite signs of pairing-order parameter[28]. Moreover, as unconventional chiral fermions carry higher even Chern numbers, theory has shown that even parity can yield a negative quantum interference correction to the quantum transport, in contrast to the positive correction in Weyl semimetals with odd parity ($C = \pm 1$), leading to distinct magnetotransport behaviour between unconventional chiral fermions and Weyl fermions[29]. Our work pioneers the exploration of the many unconventional chiral fermions predicted by theory and may provide a broader space to study the exotic physical properties of chiral fermions.

Note added: during the reviewing process of our paper, we became aware of a related study[30] showing the presence of bulk nodes in CoSi.

Online content

Any methods, additional references, Nature Research reporting summaries, source data, statements of data availability and associated accession codes are available at https://doi.org/10.1038/s41586-019-1031-8.

Received: 17 August 2018; Accepted: 8 January 2019;
Published online 20 March 2019.

1. Wan, X., Turner, A. M., Vishwanath, A. & Savrasov, S. Y. Topological semimetal and Fermi-arc surface states in the electronic structure of pyrochlore iridates. *Phys. Rev. B* **83**, 205101 (2011).
2. Weng, H., Fang, C., Fang, Z., Bernevig, B. A. & Dai, X. Weyl semimetal phase in noncentrosymmetric transition-metal monophosphides. *Phys. Rev. X* **5**, 011029 (2015).
3. Huang, S. M. et al. A Weyl Fermion semimetal with surface Fermi arcs in the transition metal monopnictide TaAs class. *Nat. Commun.* **6**, 7373 (2015).
4. Soluyanov, A. A. et al. Type-II Weyl semimetals. *Nature* **527**, 495–498 (2015).
5. Bradlyn, B. et al. Beyond Dirac and Weyl fermions: unconventional quasiparticles in conventional crystals. *Science* **353**, aaf5037 (2016).
6. Tang, P., Zhou, Q. & Zhang, S.-C. Multiple types of topological fermions in transition metal silicides. *Phys. Rev. Lett.* **119**, 206402 (2017).
7. Chang, G. et al. Unconventional chiral fermions and large topological Fermi arcs in RhSi. *Phys. Rev. Lett.* **119**, 206401 (2017).
8. Pshenay-Severin, D. A., Ivanov, Y. V., Burkov, A. A. & Burkov, A. T. Band structure and unconventional electronic topology of CoSi. *J. Phys. Condens. Matter* **30**, 135501 (2018).
9. Wang, Z. et al. Dirac semimetal and topological phase transitions in A_3Bi (A = Na, K, Rb). *Phys. Rev. B* **85**, 195320 (2012).
10. Young, S. M. et al. Dirac semimetal in three dimensions. *Phys. Rev. Lett.* **108**, 140405 (2012).
11. Wang, Z., Weng, H., Wu, Q., Dai, X. & Fang, Z. Three-dimensional Dirac semimetal and quantum transport in Cd_3As_2. *Phys. Rev. B* **88**, 125427 (2013).
12. Heikkilä, T. T. & Volovik, G. E. Nexus and Dirac lines in topological materials. *New J. Phys.* **17**, 093019 (2015).
13. Wieder, B. J., Kim, Y., Rappe, A. M. & Kane, C. L. Double Dirac semimetals in three dimensions. *Phys. Rev. Lett.* **116**, 186402 (2016).
14. Weng, H., Fang, C., Fang, Z. & Dai, X. Topological semimetals with triply degenerate nodal points in θ-phase tantalum nitride. *Phys. Rev. B* **93**, 241202 (2016).
15. Zhu, Z., Winkler, G. W., Wu, Q. S., Li, J. & Soluyanov, A. A. Triple point topological metals. *Phys. Rev. X* **6**, 031003 (2016).
16. Weng, H., Fang, C., Fang, Z. & Dai, X. Co-existence of Weyl fermion and massless triply degenerate nodal points. *Phys. Rev. B* **94**, 165201 (2016).
17. Lv, B. Q. et al. Experimental discovery of Weyl semimetal TaAs. *Phys. Rev. X* **5**, 031013 (2015).
18. Xu, S.-Y. et al. Discovery of a Weyl fermion semimetal and topological Fermi arcs. *Science* **349**, 613–617 (2015).
19. Deng, K. et al. Experimental observation of topological Fermi arcs in type-II Weyl semimetal $MoTe_2$. *Nat. Phys.* **12**, 1105 (2016).
20. Huang, L. et al. Spectroscopic evidence for a type II Weyl semimetallic state in $MoTe_2$. *Nat. Mater.* **15**, 1155 (2016).
21. Liu, Z. K. et al. Discovery of a three-dimensional topological Dirac semimetal, Na_3Bi. *Science* **343**, 864–867 (2014).
22. Lv, B. Q. et al. Observation of three-component fermions in the topological semimetal molybdenum phosphide. *Nature* **546**, 627–631 (2017).
23. Ma, J.-Z. et al. Three-component fermions with surface Fermi arcs in tungsten carbide. *Nat. Phys.* **14**, 349–354 (2018).
24. Zhang, T. et al. Double-Weyl phonons in transition-metal monosilicides. *Phys. Rev. Lett.* **120**, 016401 (2018).
25. Fang, C., Lu, L., Liu, J. & Fu, L. Topological semimetals with helicoid surface states. *Nat. Phys.* **12**, 936–941 (2016).
26. Xu, S.-Y. et al. Observation of Fermi arc surface states in a topological metal. *Science* **347**, 294–298 (2015).
27. Kargarian, M., Randeria, M. & Lu, Y.-M. Are the surface Fermi arcs in Dirac semimetals topologically protected? *Proc. Natl Acad. Sci. USA* **113**, 8648–8652 (2016).
28. Qi, X.-L., Hughes, T. L. & Zhang, S.-C. Topological invariants for the Fermi surface of a time-reversal-invariant superconductor. *Phys. Rev. B* **81**, 134508 (2010).
29. Dai, X., Lu, H.-Z., Shen, S.-Q. & Yao, H. Detecting monopole charge in Weyl semimetals via quantum interference transport. *Phys. Rev. B* **93**, 161110 (2016).
30. Takane, D. et al. Observation of chiral fermions with a large topological charge and associated Fermi-arc surface states in CoSi. *Phys. Rev. Lett.* **122**, 076402 (2019).

Acknowledgements We thank Y. Zhong and J. Guan for assistance with the RHEED measurements. We thank H. Yao, H. Lu and Z. Wang for discussions. We thank N. B. M. Schröter, A. Chikina and V. N. Strocov for assistance with the ARPES measurements at the SLS. This work was supported by the Ministry of Science and Technology of China (2016YFA0401000, 2015CB921000, 2016YFA0300600, 2016YFA0300504, 2016YFA0302400, 2018YFA0305700 and 2017YFA0302901), the National Natural Science Foundation of China (11622435, U1832202, 11474340, 11822412, 11574371, 11674369, 11574394, 11774423 and 11774399), the Chinese Academy of Sciences (QYZDB-SSW-SLH043, XDB07000000 and XDB28000000), the Science Challenge Project (TZ2016004), the K. C. Wong Education Foundation (GJTD-2018-01), the Beijing Natural Science Foundation (Z180008) and the Beijing Municipal Science and Technology Commission (Z171100002017018, Z181100004218005 and Z181100004218001). Y.H. acknowledges support by the CAS Pioneer Hundred Talents Program (type C). Z. Li acknowledges support by the National Postdoctoral Program for Innovative Talents (BX20170012).

Author contributions T.Q. and Y. Sun supervised the project. Z.R., H. Li and T.Q. performed the ARPES measurements with the assistance of B.F., W.F., J.L. and Y.H.; Z.R., C.T. and Y. Sun processed the sample surfaces with the assistance of Z. Liu and Y.L.; T.Z. and H.W. performed ab initio calculations; S.T., C.L., H. Lei, L.W., Y. Shi and Z. Li synthesized the single crystals; Z.R, H. Li, T.Q. and Y. Sun analysed the experimental data; Z.R., T.Z., T.Q. and Y. Sun plotted the figures; T.Q., C.F. and H.D. wrote the manuscript.

Competing interests The authors declare no competing interests.

Additional information
Reprints and permissions information is available at http://www.nature.com/reprints.
Correspondence and requests for materials should be addressed to H. Lei, Y. Sun or T.Q.
Publisher's note: Springer Nature remains neutral with regard to jurisdictional claims in published maps and institutional affiliations.

METHODS

Sample synthesis. Single crystals of CoSi were grown by the chemical vapour transport method. Co and Si powders in 1:1 molar ratio were put in a silica tube with a length of 200 mm and an inner diameter of 14 mm. Then, 200 mg I_2 was added into the tube as a transport reagent. The tube was evacuated to 10^{-2} Pa and sealed under vacuum. The tubes were placed in a two-zone horizontal tube furnace and the temperatures of the source and growth zones were raised to 1,173 K and 1,273 K, respectively, for two days and then held there for seven days. Shiny crystals with lateral dimensions of up to several millimetres were obtained.

Angle-resolved photoemission spectroscopy. ARPES measurements were performed at the 'Dreamline' beamline of the Shanghai Synchrotron Radiation Facility (SSRF) with a Scienta Omicron DA30L analyser and at the Advanced Resonant Spectroscopies (ADRESS) beamline at the Swiss Light Source (SLS) with a SPECS analyser. All the ARPES data shown were collected at SSRF. To obtain atomically flat surfaces for the ARPES measurements, we polished the (111) and (001) surfaces of single crystals, and then repeatedly sputtered the surfaces and annealed the samples until clear RHEED patterns appeared.

Band structure calculations. First-principles calculations were performed using density functional theory[31] within the Perdew–Burke–Ernzerhof exchange correlation[32] and implemented in the Vienna ab initio simulation package (VASP)[33]. A $20 \times 20 \times 20$ k-mesh was used in the BZ for the self-consistent calculations, and all the calculations were made considering absence of SOC. Three-dimensional FS calculations were performed using the tight-binding model of bulk CoSi, which was obtained from maximally localized Wannier functions[34]. The experimental values of the atomic sites and the lattice constant[35] $a = 4.445$ Å were used in our calculations.

Data availability

Materials and additional data related to this paper are available from the authors upon request.

31. Hohenberg, P. & Kohn, W. Inhomogeneous electron gas. *Phys. Rev.* **136**, B864–B871 (1964).
32. Perdew, J. P., Burke, K. & Ernzerhof, M. Generalized gradient approximation made simple. *Phys. Rev. Lett.* **77**, 3865–3868 (1996).
33. Kresse, G. & Furthmüller, J. Efficient iterative schemes for ab initio total-energy calculations using a plane-wave basis set. *Phys. Rev. B* **54**, 11169–11186 (1996).
34. Marzari, N. & Vanderbilt, D. Maximally localized generalized Wannier functions for composite energy bands. *Phys. Rev. B* **56**, 12847–12865 (1997).
35. CoSi crystal structure. *Inorganic Solid Phases* https://materials.springer.com/isp/crystallographic/docs/sd_0378292 (Springer Materials, 2016).